


Article

Microplasma-Enabled Sustainable Synthesis of Nitrogen-Doped Graphene Quantum Dots for Sensitive Detection of 4-Nitrophenol

Michael Ryan Rahardja, Darwin Kurniawan *  and Wei-Hung Chiang * 

Department of Chemical Engineering, National Taiwan University of Science and Technology, Taipei 10607, Taiwan; m11106803@mail.ntust.edu.tw

* Correspondence: d10806801@mail.ntust.edu.tw (D.K.); whchiang@mail.ntust.edu.tw (W.-H.C.)

Abstract: 4-nitrophenol (4-NP) is one of the organic pollutants that can come up from pesticides, explosives, dyes, and pharmaceutical industries. Since it can be extremely harmful to humans and other living organisms, it is crucial to have a system that can effectively detect the presence of 4-NP. Here, we report the microplasma synthesis of nitrogen-doped graphene quantum dots (N-GQDs) for fluorescence-based detection of 4-NP. Through Förster resonance energy transfer (FRET) between donor N-GQDs to the acceptor 4-NP, synthesized N-GQDs can be employed for the detection of 4-NP starting from 0.5 to 100 μM with a limit of detection as low as 95.14 nM. 4-NP detection also demonstrates remarkable stability over all pH values and wide temperatures (10–60 $^{\circ}\text{C}$), indicating the high possibility for robust organic pollution monitoring. Our work provides insight into a simple, fast, and environmentally friendly method for synthesizing N-GQDs at ambient conditions usable for environmental nanosensors.

Keywords: 4-nitrophenol; nitrogen-doped graphene quantum dots; microplasmas; pollution monitoring; nanotechnology



Citation: Rahardja, M.R.; Kurniawan, D.; Chiang, W.-H.

Microplasma-Enabled Sustainable Synthesis of Nitrogen-Doped Graphene Quantum Dots for Sensitive Detection of 4-Nitrophenol. *Chemosensors* **2023**, *11*, 390. <https://doi.org/10.3390/chemosensors11070390>

Academic Editor: Sherif Moussa

Received: 6 June 2023

Revised: 7 July 2023

Accepted: 10 July 2023

Published: 13 July 2023



Copyright: © 2023 by the authors. Licensee MDPI, Basel, Switzerland. This article is an open access article distributed under the terms and conditions of the Creative Commons Attribution (CC BY) license (<https://creativecommons.org/licenses/by/4.0/>).

1. Introduction

4-nitrophenol (4-NP) is one of the organic pollutants that can come up from pesticides, explosives, dye, and pharmaceutical industries [1]. Owing to its carcinogenicity, 4-NP is dangerous to people or other living things, and drinking water is the pathway for 4-NP poisoning to humans [2]. The maximum acceptable level of 4-NP in drinking water is 60 $\mu\text{g}/\text{L}$ or similar to $\sim 0.43 \mu\text{M}$ [1–3]. If ingested by people, it poses major health risks including methemoglobinemia, headaches, and liver or kidney damage [1]. Recently, a number of analytical techniques have been applied for the detection of 4-NP, including fluorimetry [4,5], spectrophotometry [6,7], gas and liquid chromatography [8,9], liquid chromatography-tandem mass spectrometry [10], electrochemistry [11–13], photoelectrochemistry [14], high-performance liquid chromatography [15], and the fuel cell-based sensing platform [16,17]. These techniques, however, have certain limitations, i.e., expensive materials, high cost of experimental procedure, complexity, and being time consuming, which limit their broad applications [1]. The fluorescence-based approach, on the other hand, is practical, quick, inexpensive, highly sensitive, and selective [1,2].

Graphene quantum dots (GQDs) are zero-dimensional carbon-based materials constructed of single- or multilayer graphitic structure with a lateral dimension that is not greater than 100 nm [18,19]. GQDs exhibit unique photoluminescence (PL) properties arising from the quantum confinement and edge effects. Coupled with biocompatibility, low toxicity, and photostability, GQDs are useful for many applications including sensing, imaging, optoelectronics, energy generation and storage, and catalysis [20,21]. Doping with heteroatoms such as B, N, P, and S can improve the electrical and chemical characteristics of GQDs [22–27]. Among them, N doping is the most utilized technique in order to

improve the photoemission of GQDs. This is due to the fact that N will bind to carbon, shifting the Fermi level upward and releasing electrons into the conduction band, which can significantly increase the PL emission of GQDs [28]. Several applications for N-doping include sensing [29], bioimaging [30–32], and catalysis [33].

The synthesis of nitrogen-doped GQDs (N-GQDs) can be divided into two general strategies including direct synthesis from carbon and nitrogen precursors and postprocessing of N doping into pre-synthesized GQDs [34]. Postgrowth doping usually requires high temperatures and pressures, strong acids and bases, and a long reaction time. Meanwhile, direct synthesis is usually more preferable and can be achieved using top-down and bottom-up approaches. The former involves the exfoliation of larger N-doped carbon materials (e.g., graphite, graphene, carbon nanotube) into N-GQDs, whereas the latter involves the formation of N-GQDs via carbonization, pyrolysis, and step-wise chemical reaction of small nitrogen-containing hydrocarbons [34,35]. However, overall, the process still requires the use of high temperatures, strong acids, toxic chemicals, cumbersome procedures, and long reaction times. There is a need to develop a simpler yet rapid and environmentally friendly method to synthesize N-GQDs.

Here, we report the microplasma synthesis of N-GQDs from chitosan for 4-NP detection. As a biomass derived from a natural resource, chitosan is biocompatible and biodegradable, which enables the sustainable synthesis of N-GQDs [36,37]. Microplasmas as one-dimensional discharges smaller than one millimeter in scale possess a high density of reactive species (radicals, ions, electrons, and photons), which are useful for the synthesis of GQDs, metal nanoparticles, and composites [38–44]. Owing to sp^2 hybridization, N-GQDs are capable of demonstrating strong π - π interaction with 4-NP, and subsequently lead to Förster resonance energy transfer (FRET) from N-GQDs to 4-NP. As a result, the synthesized N-GQDs are usable for 4-NP detection with a broad linear range from 0.5–100 μ M with a limit of detection (LoD) of 95.14 nM. Moreover, 4-NP detection using N-GQDs is stable over the whole pH range and a wide temperature range (10–60 $^{\circ}$ C), suggesting a robust pollutant nanosensor with a high potential for real application. Our work provides insight into the simple, rapid, environmentally friendly, and sustainable synthesis of N-GQDs at ambient conditions for environmental nanosensors.

2. Materials and Methods

2.1. Materials and Reagents

Sigma Aldrich Co., Ltd. (Taipei, Taiwan) provided the chitosan (low molecular weight, 50–190 kDa, CAS: 9012-76-4) and sodium hydroxide (NaOH, 98%, CAS: 1310-73-2) pellets. Acetic acid glacial ($\geq 99.7\%$, CAS: 64-19-7) was bought from Fisher Scientific part of Thermo Fisher Scientific (Taipei, Taiwan). 4-nitrophenol (4-NP, 99%, CAS: 100-02-7) was obtained from Alfa Aesar by Thermo Fisher Scientific (Taipei, Taiwan). Guv Team International Co., Ltd. (New Taipei, Taiwan) supplied the Pt foil (99.95%, 20 mm \times 20 mm \times 0.1 mm).

2.2. Synthesis of N-GQDs

Chitosan solution was prepared by dissolving 300 mg of low molecular weight chitosan with 19.6 mL of deionized water and 0.4 mL of 5 M acetic acid solution. The solution was added with 20 mL of DI water again to reduce the viscosity. The final concentration of chitosan precursor solution was 62.5 μ M. Ten milliliters of chitosan precursor solution was taken and subjected to microplasma treatment at 9.6 mA fixed discharge current for 60 min to synthesize the N-GQDs (Figure 1).

2.3. Purification of N-GQDs

After the synthesis, the plasma-treated solution was neutralized with 1 M NaOH (\sim pH 7.4). Then, acetone was added to the solution to precipitate the unreacted chitosan. The volume ratio of the added acetone to the plasma-treated solution was 2 to 1. Once the chitosan had been precipitated, the suspension was vacuum-filtrated to remove the chitosan precipitate. The obtained solution was further subjected to rotary evaporation (Eyela, Tokyo, Japan) at low

pressure (~5 Pa) to remove the acetone. The rotary evaporator was equipped with a continuous cooling system operated at $-13\text{ }^{\circ}\text{C}$. During the evaporation process, half of the sample vial was immersed in a water bath with a fixed temperature at $30\text{ }^{\circ}\text{C}$. After acetone removal, the resulting N-GQD solution was subjected to dialysis (CE tubing 500–1000 Da) against DI water for 24 h to remove the salt and buffer formed by the neutralization process. The outer dialysis solution was replaced with fresh DI water every 6 h. Then, the obtained purified N-GQD solution was rotary-evaporated until around 0.2 mL solution remained. Around 3 mL of ethanol was added to the N-GQD solution to precipitate the N-GQDs, followed by rotary evaporation again to obtain fine N-GQD powder. To prevent water moisture absorption, the N-GQD powder was stored in a vacuum chamber filled with silica gel for further usage.

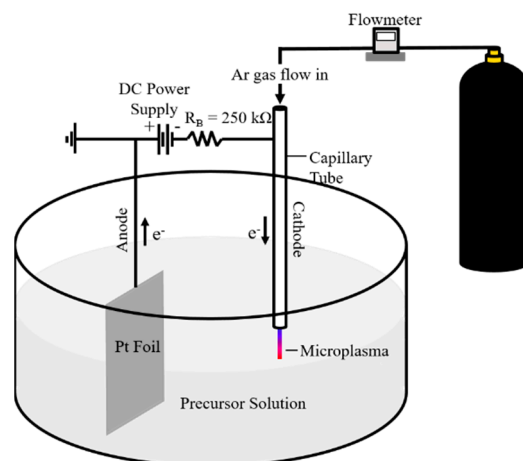


Figure 1. Microplasma configuration for N-GQD synthesis.

2.4. Characterization of N-GQDs

Absorption spectra of N-GQDs was recorded using Jasco V676 spectrophotometer (Tokyo, Japan). A matched pair of quartz cuvettes with a path length of 1 cm were used for the measurements and baseline correction was performed before every measurement. PL measurement was conducted using Horiba Jobin Yvon Nanolog-3 spectrofluorometer (Kyoto, Japan). The acquired PL spectra were scaled based on the observed excitation power. A field emission gun TEM (FEI Tecnai G2 F-20 S-TWIN, Oregon, United States & JEOL JEM-2100F, Tokyo, Japan) with an accelerating voltage of 200 kV was used to conduct the TEM experiments. The TEM samples were made by solution dry-casting N-GQDs onto copper grids (400 mesh, Ted Pella Inc., California, United States) covered with carbon. Using the software Digital Micrograph 3.7, the particle size distributions and lattice spacing of N-GQDs were determined. An ESCALAB Xi+ (Thermo Fisher Scientific, Winsford, United Kingdom) with monochromatic Al $K\alpha$ X-ray radiation as the source gun type, a pass energy of 150.0 eV, and a beam size of 650 μm was used to conduct the XPS experiments. A He-Cd laser (wavelength: 325 nm) -equipped LabRAM HR Evolution spectrometer from Horiba (Kyoto, Japan) was used to perform the Raman measurement with spectral resolution of 1.0 cm^{-1} . The purified N-GQDs were drop-casted on Si wafer followed by drying at $35\text{ }^{\circ}\text{C}$. To prevent sample damage from the laser, the laser power was regulated and kept at 0.1 mW. Prior to the test, the Raman spectrometer was calibrated using a silicon wafer that peaks at Raman shift of 520 cm^{-1} .

2.5. 4-NP Sensing

The optimal incubation time was determined by adding 4-NP solution to the N-GQD solution and then measuring the response using a PL spectrophotometer under 330 nm excitation wavelength. To prevent dilution effect during the PL measurement, the volume of the specimen was kept at 3 mL throughout the whole experiments. First, 0.3 mg/mL of N-GQD and 300 μM of 4-NP mother solutions were prepared in DI water. Then, 1 mL of the N-GQD solution with a concentration of 0.3 mg/mL was taken and moved into a quartz

cuvette. A quantity of 1.5 mL DI water was added into the cuvette, followed by the addition of 0.5 mL of 300 μ M 4-NP solution into the cuvette. The incubation time was started right after the final addition of 4-NP and was set from 0 min to 12 min with an interval of 3 min for every PL measurement. The final concentrations of the 4-NP and N-GQDs were 50 μ M and 0.1 mg/mL, respectively. Once the optimal incubation time had been obtained, the 4-NP detection was conducted by measuring the PL of the mixtures containing a fixed concentration of N-GQDs (0.1 mg/mL) but with different concentrations of 4-NP ranging 0.5–150 μ M. All the mixtures were prepared by fixing the N-GQDs volume to be 1 mL in every specimen, but the amount of the added DI water and 4-NP was adjusted to realize different concentrations of 4-NP in the final specimen mixtures (Table 1). The highest emission intensity of each spectrum was selected for the data analysis and processing.

Table 1. Specimen preparation condition for the detection of 4-NP with N-GQDs.

0.3 mg/mL N-GQD Mother Solution	Added Amounts (mL)		Final Concentrations	
	DI Water	300 μ M 4-NP Mother Solution	N-GQDs (mg/mL)	4-NP (μ M)
1.000	1.995	0.005	0.1	0.5
	1.990	0.01		1
	1.975	0.025		2.5
	1.950	0.05		5
	1.925	0.075		7.5
	1.900	0.1		10
	1.875	0.125		12.5
	1.833	0.1667		16.67
	1.750	0.25		25
	1.667	0.3333		33.33
	1.583	0.4167		41.67
	1.500	0.5		50
	1.433	0.5667		56.67
	1.250	0.75		75
	1.000	1		100
	0.750	1.25		125
	0.500	1.5		150

2.6. pH Stability

A 0.1 M solution of phosphate buffer saline (PBS) was mixed with 1 M of HCl to prepare acidic PBS solution, while 1 M of NaOH was added to adjust the pH to basic. The different pH solutions were then mixed with the N-GQD and 4-NP solutions and subjected to PL measurement under 330 nm excitation wavelength. The highest emission intensity of each spectrum was selected for the data analysis and processing.

2.7. Temperature Stability

A mixture of 4-NP and N-GQD solution was immersed in a water bath with a temperature range from 10 to 60 $^{\circ}$ C. The temperature during the PL measurement was maintained by continuously flowing water at the respective temperature through the PL stage channel. The PL was performed under 330 nm excitation wavelength. The highest emission intensity of each spectrum was selected for data analysis and processing.

3. Results and Discussion

3.1. Synthesis of N-GQDs

Figure 2a shows an absorption spectra of chitosan precursor solution before and after microplasma treatment. The precursor solution (black line) does not show any absorption peak; however, after the microplasma treatment at 9.6 mA for 1 h, a broad absorption from 300 to 400 nm can be observed (red line). This absorption can be assigned to $n \rightarrow \pi^*$ transitions either C=O bonds or C-O bonds [42,45]. The highest absorption peak at 281 nm is attributed to the $\pi \rightarrow \pi^*$ transition of C=C structures [45], and $n \rightarrow \pi^*$ transitions of C-N bonds [46]. It is obvious that the absorption band is wider than the previously reported pristine GQDs [47], which might be attributed to N doping. Unlike the excitation-independent emission of pristine GQDs [47], the PL map of N-GQDs in Figure 2b shows that the N-GQDs demonstrate excitation-dependent emission with local maxima at 492 and 410 nm of those emission and excitation, respectively. Note that the strongest PL excitation at 410 nm despite its minimal absorption in that particular wavelength can be attributed to the surface emissive states within the bandgap of N-GQDs. These surface-emissive states are promoted by the presence of oxygen and nitrogen functionalities, inducing the $n \rightarrow \pi^*$ transitions that are responsible for the PL.

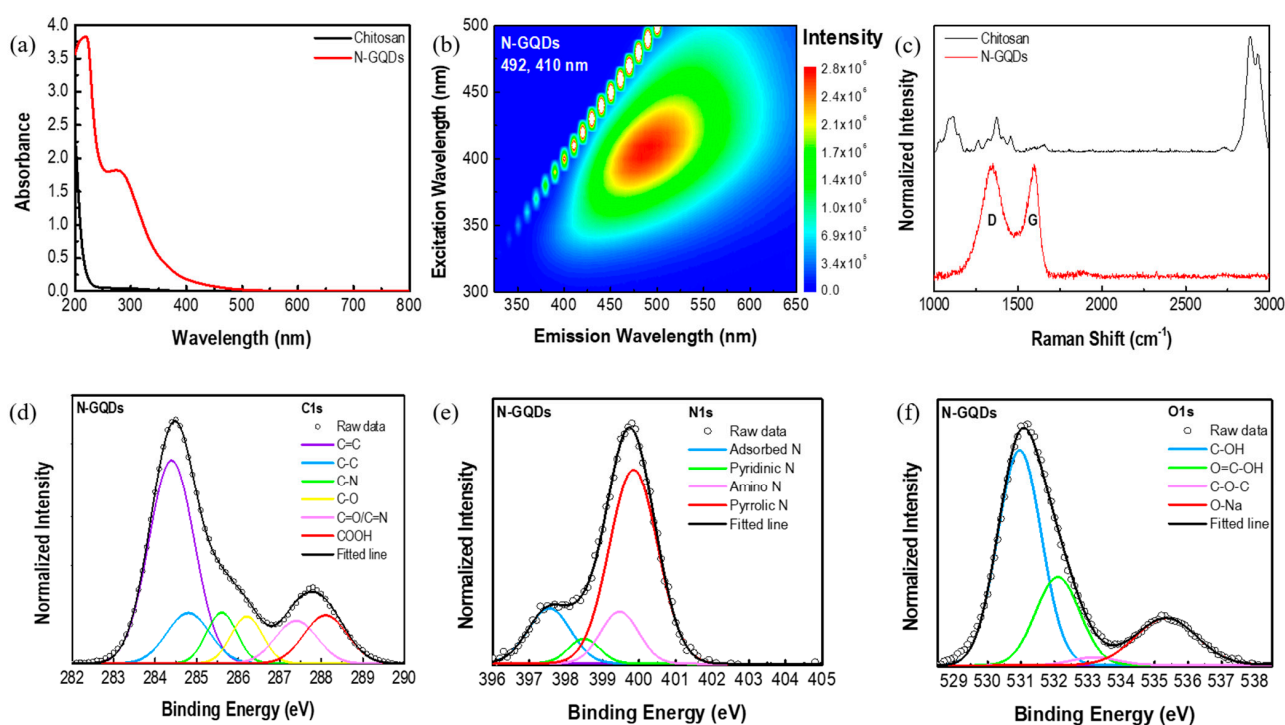


Figure 2. Spectroscopic characterizations of N-GQDs. (a) UV-Visible absorption spectra of N-GQDs and chitosan. (b) PL map, (c) Raman spectrum, and high resolution XPS measurement on (d) C1s, (e) N1s, and (f) O1s of N-GQDs.

The Raman study also confirms that N-GQDs were produced by showing two prominent peaks at 1350 and 1597 cm^{-1} corresponding to the D- and G-band of N-GQDs, respectively (Figure 2c, red line). The D-band originates from the N-doping that causes structural disorder in the graphene lattice, a vacancy spot owing to non-graphitic N-doping, and edges. This D-band also seems to be higher when compared to the D-band of pristine GQDs reported previously [47]. On the other hand, the G-band alludes to the high crystalline graphene structure present in N-GQDs [48]. Furthermore, when compared to the Raman spectra of chitosan (Figure 2c, black line), there is no peak found after 1500 cm^{-1} in the N-GQD solution. This indicates that no chitosan was left in the solution after the process and purification, resulting in high-purity N-GQDs.

The existence of functional groups in N-GQDs can be investigated using X-ray photoelectron spectroscopy (XPS). The C1s peak of N-GQDs (Figure 2d) incorporates vari-

ous bindings, including C=C (284.4 eV), C-C (284.8 eV), C-N (285.6 eV), C-O (286.2 eV), C=O/C=N (287.4 eV), and COOH (288.1 eV). Furthermore, the deconvoluted N1s peak (Figure 2e) consists of adsorbed N (397.6 eV), pyridinic N (398.5 eV), amino N (399.5 eV), and pyrrolic N (399.9 eV). The occurrence of N1s peak in the N-GQDs further clarify the existence of N doping in the GQD. Moreover, the N-GQDs are also enriched with oxygen-containing-groups, proven by the O1s peak (Figure 2f) that shows C-OH at 531 eV, O=C-OH at 532.1 eV, C-O-C at 532.2 eV. The O-Na at 535.3 eV is due to the NaOH added to neutralize the solution for purification purposes.

To understand the morphologies of synthesized N-GQDs, transmission electron microscopy (TEM) was performed on the N-GQDs. Figure 3a shows the particle-like nanostructures with no agglomeration. In addition, Figure 3b depicts the size distribution histogram of N-GQDs with an average size of 6.2 ± 1.0 nm based on 55 different particles fitted with standard normal distribution. Being compared to pristine GQDs, the particle size of N-GQDs were slightly bigger than pure GQDs. According to our previous work [47], the particle size of GQDs derived from fructose, citric acid, and starch were 4.5 ± 1.7 , 3.6 ± 0.3 , and 4.1 ± 0.8 nm, respectively. It is possible that the nitrogen atoms being incorporated into the graphene lattice can cause defects and distortion of the carbon network, resulting in larger particle size. However, further study still needs to be conducted to confirm the above hypothesis. On the other hand, the high-resolution TEM presented in Figure 3c reveals the lattice spacing of the N-GQD particle, while the diffraction pattern is shown in the fast Fourier transform (FFT) image (Figure 3d, inset). By taking the inverse FFT, a clear lattice spacing of 0.23 nm was obtained, which corresponds to the (1120) plane of graphene [49,50].

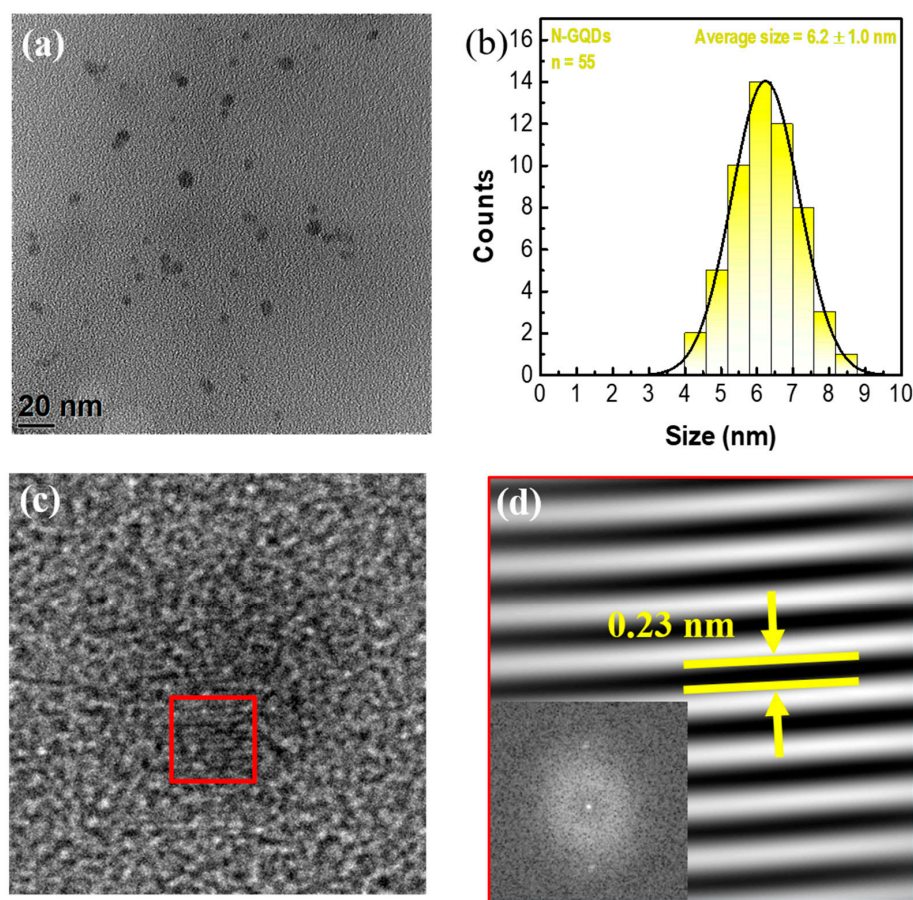


Figure 3. Morphological characterization of N-GQDs. (a) TEM image, (b) size distribution histogram, (c) HRTEM, and (d) inverse FFT images of N-GQDs. Inset shows the FFT image.

3.2. 4-NP Sensing with N-GQDs

Figure 4a demonstrates around more than 50% of the N-GQDs' PL intensity is quenched right after the addition of 4-NP. To understand the optimal incubation time, the PL was further measured with a 3 min time interval until 12 min. The summarized result in Figure 4b shows that the PL seems to remain constant from 0 to 12 min, implying a rapid detection system. Although the PL was directly quenched and remained constant after the addition of 4-NP, 3 min was chosen as the incubation time throughout the experiment for better consideration for the later pH and temperature stabilities. As shown in Figure 4c, the PL intensity of the N-GQDs decreases as the concentration of 4-NP increases. By taking a ratio between the PL intensity of N-GQDs in the absence and presence of 4-NP, a linear correlation was obtained in the range of 0.5–100 μM with a limit of detection (LoD) of 95.14 nM based on the threefold signal-to-noise ratio (Figure 4d). Compared with the previous result [51], the synthesized N-GQDs possess 50 nM lower LoD than the reported pristine GQDs, suggesting that the presence of N doping in the GQDs might play a role in the increased sensitivity, yet further study still needs to be conducted. A gradual emission intensity decrement of N-GQDs with increasing concentration of 4-NP can also be visually observed under 365 nm UV light (Figure 4d, inset).

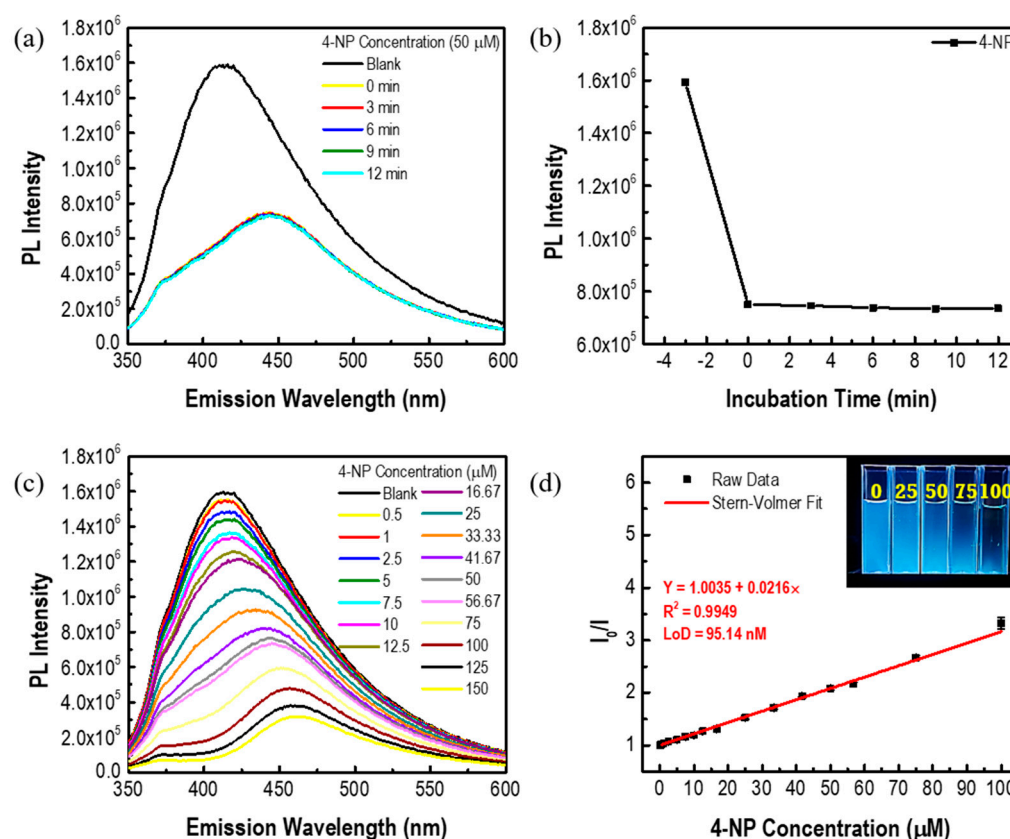


Figure 4. PL-based detection of 4-NP with N-GQDs. (a) PL spectra of 4-NP at different incubation times. (b) Summarized PL intensities of 4-NP at different incubation times. (c) PL spectra of 4-NP at different concentrations. (d) PL intensity ratio of N-GQDs in the absence (I_0) and presence of 4-NP at different concentrations (I) under 330 nm excitation wavelength. Inset shows the visual image of N-GQD solution under 365 nm UV irradiation in the presence of 4-NP ranging from 0, 25, 50, 75, and 100 μM .

To understand the robustness of the N-GQDs for actual pollutant sensing, pH and temperature stable tests were conducted. Figure 5a displays the normalized PL spectra of N-GQDs containing 50 μM of 4-NP at different pH values. Despite the red-shifted PL spectra at alkaline condition, PL quenching of around 50% can still be retained. The red-shifted PL spectra at alkaline condition may plausibly be caused by the deprotonation of the

surface functional groups of the N-GQDs. The result in Figure 5a is further summarized into PL intensity ratios (Figure 5b), demonstrating a relatively stable PL sensing performance at different pH values. In addition, the temperature stability test during the 4-NP detection also demonstrates a stable performance ranging from 10 to 60 °C (Figure 5c,d).

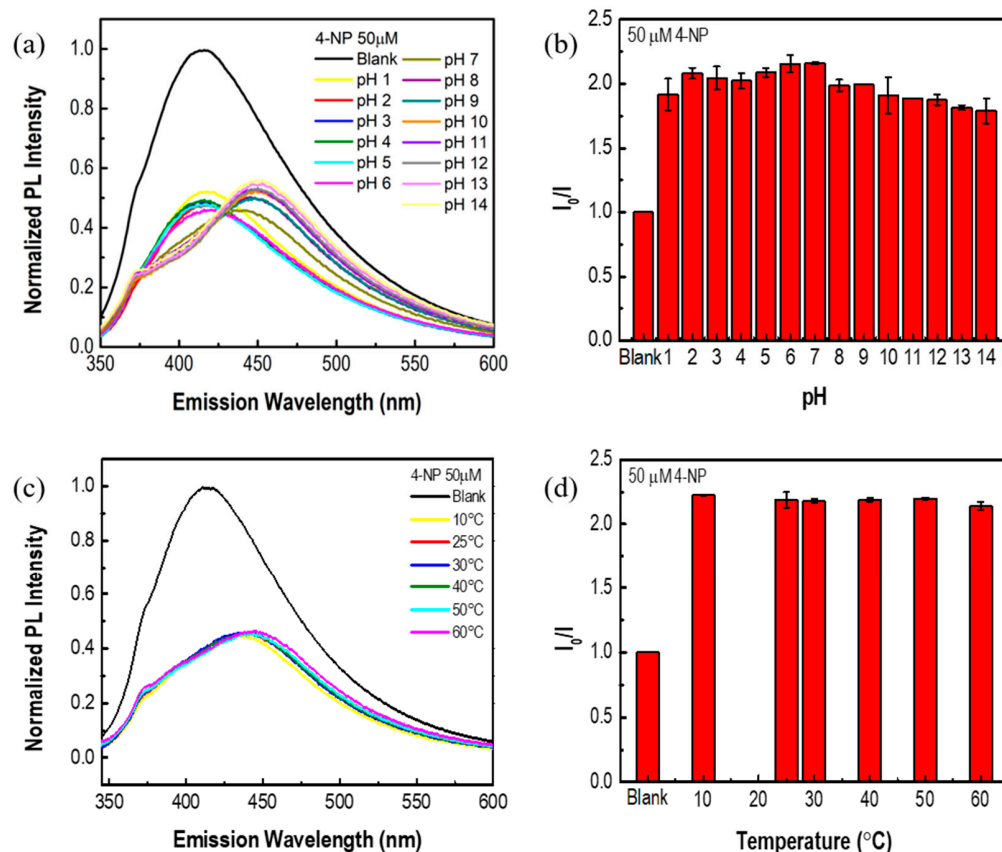


Figure 5. Stability of N-GQDs for 4-NP detection. PL spectra of N-GQDs with addition of 4-NP at different (a) pH and (c) temperatures. Bar charts of I_0/I ratio of 4-NP at different (b) pH and (d) temperatures.

In addition, the 4-NP sensing mechanism of N-GQDs was also investigated. Figure 6a shows the absorption spectra of 4-NP before and after the addition of N-GQDs. The absorption peak observed at 318 nm corresponds to the 4-NP structure (Figure 6a), while the absorption shoulder around 400 nm can be attributed to the ionized state of 4-NP ($-OH$ to $-O^-$). After the addition of N-GQDs, 4-NP is completely deprotonated to 4-nitrophenolate ion [2], causing the decrement and increment in absorption at 318 and 400 nm, respectively. The shifted absorption peak of 4-NP to 400 nm causes its absorption spectrum to be well overlapped with the PL emission spectrum of N-GQDs (Figure 6b). As a consequence, FRET (Förster resonance energy transfer) can occur [50–52], in which the donor fluorophore (N-GQDs) and acceptor fluorophore (4-NP) interact non-radiatively to form a dipole-dipole synergy [52] that results in the PL quenching phenomenon of N-GQDs in the presence of 4-NP.

However, FRET can only occur when the distance between the donor and acceptor is less than 10 nm [53]. Note that the long conjugated sp^2 domain of N-GQDs can promote strong π - π interaction with other aromatic compounds, while the presence of surface functional groups in the N-GQDs can contribute to hydrogen bonding with other molecules. Therefore, π - π interaction and hydrogen bonding can bring the 4-NP molecules and N-GQD particles in close proximity to enable the FRET phenomenon. The occurrence of hydrogen bonding between N-GQDs and 4-NP can be perceived from the gradual red-shift of N-GQD PL emission with increasing 4-NP concentration (Figure 4c) [54]. Figure S1 confirms that the red-shifted PL emission of N-GQDs in the presence of 4-NP is not contributed by the emission of 4-NP, because 4-NP does not fluoresce.

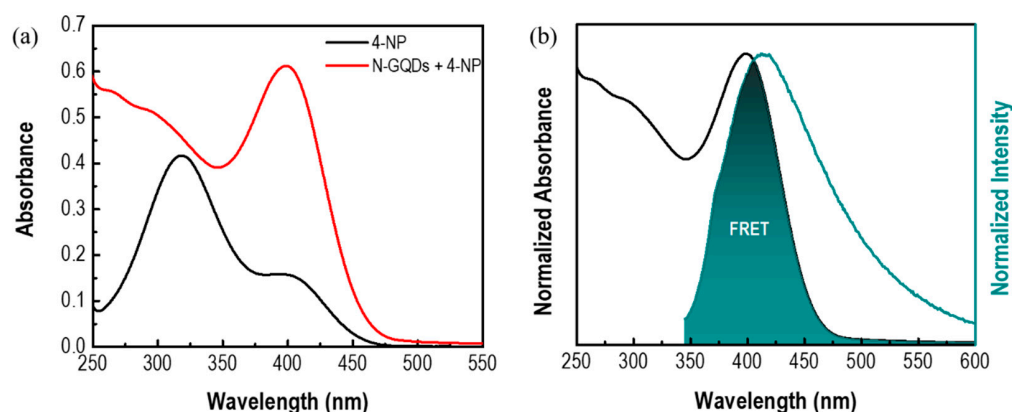


Figure 6. Sensing mechanism of 4-NP. (a) Absorption spectra of 4-NP in the absence (black line) and presence of N-GQDs (red line). (b) The spectral overlap between the 4-NP absorption and N-GQDs emission spectra showing FRET phenomenon.

Besides FRET, a previous study revealed that the sensing mechanism of 4-NP can be attributed to the electron transfer due to the strong electron withdrawing ability of the nitro group [2] and inner filter effect (IFE) [1]. To confirm the possibility of electron transfer, we subjected our N-GQDs with other nitroaromatic compounds, including 4-nitroaniline (4-NA), 1, 5-dinitronaphthalene, and *p*-nitrochlorobenzene (Figure S2). It is apparent that pronounced PL quenching was observed in the presence of 4-NP and 4-NA but not in 1, 5-dinitronaphthalene and *p*-nitrochlorobenzene (Figure S3). This result suggests that although electron transfer may not be the main regulating mechanism, it probably still occurs in tandem with the FRET phenomenon.

In the IFE case, the PL quenching occurs due to the partial absorption of the excitation photons by the analyte, induced by the strong analyte absorption in the corresponding excitation wavelength [53]. To confirm the possibility of IFE, the detection of 4-NP was further conducted under different excitation wavelengths from 300 to 350 nm and the result is presented in Figure S4. It can be observed that the highest quenching ratio occurs at 320 nm excitation, which is close to the maximum absorption peak of 4-NP at 318 nm (Figure 6a). There is a high tendency that IFE can also occur and assist the PL quenching of N-GQDs in the presence of 4-NP.

In addition, it is worthy to highlight that despite the simplicity and environmental-friendliness of our synthesis process, the produced N-GQDs are usable for 4-NP detection with comparable performance to other studies (Table 2). Most of the synthesis processes still require the use of high temperature, long reaction time, and/or complex chemical precursors, which can limit their practicality in real applications. Moreover, our microplasma process can be scaled up by constructing a microplasma array coupled with the integration of microfluidic devices [55,56], bearing great potential for industrial-scale applications.

Table 2. Comparison of different probes for PL-based detection of 4-NP.

No.	Precursor	Synthesis Method	Reaction Parameters	Materials	Linear Range (μM)	R^2	LoD (nM)	Ref.
1	Chitosan	Microplasma	1 h 9.6 mA	N-GQDs	0.5–100	0.995	95.14	This study
2	Hydroquinone and EDA	Hydrothermal	2 h 50 °C	PCDs	0.5–60	0.991	260	[1]
3	Apple seeds	Pyrolysis	1 h 300 °C	CNDs	0.05–53	0.994	13	[57]
4	Coumarin-FL-IL, EGDMA, IL [V ₂ C ₄ (mim) ₂][(PF ₆) ₂]	Polymerization	15 min	Coumarin-based FL-MIPIL	0.001–7.5	0.992	0.5	[58]
	FL-MIPIL and EGDMA	Polymerization	15 min	Coumarin-based FL-EGDMA-MIP	0.05–7.5	0.991	10	

Table 2. Cont.

No.	Precursor	Synthesis Method	Reaction Parameters	Materials	Linear Range (μM)	R ²	LoD (nM)	Ref.
5	PA and EDA	One Pot hydrothermal	6 h 200 °C	N-CDs	0.1–100	0.999	17	[59]
6	CA and 3-MPA	Pyrolysis	45 min 200 °C	S-GQDs	0.01–1 1–200	0.979 0.984	0.7	[54]
7	BSA and HAuCl ₄	Incubation	12 h 37 °C	Dual-emissive GNCs	0.05–5	0.991	13.8	[60]
8	H ₄ BF ₄ N and C ₆ H ₅ Na ₃ O ₇	Hydrothermal	5 h 200 °C	N-GQDs	0–20	0.999	290	[61]
9	Polymethylvinylsiloxane P500 and 4-Bromotriphenylamine	Heck reaction	48 h	BpaP	0–50	0.940	600	[62]
	2,4,6,8-tetramethyltetravinylcyclotetra-siloxane and 4-Bromotriphenylamine	Heck reaction	48 h	BpaD	0–50	0.935	230	
10	UiO-66 nanocrystals and amine-CQDs	Immersion	12 h Room temperature	Amine-CQDs@UiO-66	0.01–20	0.990	3.5	[63]
11	<i>Bacillus cereus</i> MYB41-22	Hydrothermal	12 h 200 °C	CDs-BC	0.3–6.5 6.5–30	0.999 0.991	110	[64]
12	Sweet flag (<i>Acorus calamus</i>)	Microwave irradiation	25 min	CDs	0–14.28	0.997	207	[65]
13	Crayfish shells	Hydrothermal	8 h 180 °C	CDs	0–50	0.996	160	[66]
14	CA and O-PDA (CQDs); PTMS and TEOS (MIP@CQDs)	Hydrothermal (CQDs); Sol-gel imprinting (MIP@CQDs)	8 h, 160 °C (CQDs); 12 h (MIP@CQDs)	MIP@CQDs	0–144	0.995	410	[67]
15	1-propyl-3-methylimidazol and 1,3-dibromopropane	Mixing and heating	20 h 60 °C	[C ₃ (MIM) ₂] [NA] ₂	1–500	0.999	300	[68]
16	Sea rice	Mild oxidation	8 h 26 °C	GQDs	0–1000	0.996	34	[69]
17	Glucose (CDs); Eu(NO ₃) ₃ ·6H ₂ O, 1,10-phen, H ₄ btec, NaOH (Eu-MOF)	Hydrothermal carbonization (CDs);	3 h, 160 °C (CDs); 48 h, 140 °C (Eu-MOF)	CDs@Eu-MOF	0–68.96	0.996	40.04	[70]
		Hydrothermal (Eu-MOF)		CDs@Eu-MOF/PVDF film	0–129.3	0.998	72.41	
18	DAPH and DAMO	One-step room temperature synthesis	3 h Room temperature	SiNPs	0.05–600	0.983	3.3	[71]
19	Eu(NO ₃) ₃ · 6H ₂ O, Zn(CH ₃ COO) ₂ ·2H ₂ O, and H ₃ BTC	Solvothermal	24 h 120 °C	Zn(Eu)-MOF	0–129.3	0.977	3154.9	[72]
	Eu(NO ₃) ₃ · 6H ₂ O, Zn(CH ₃ COO) ₂ ·2H ₂ O, H ₃ BTC, and PAN	In-situ growth and mixed spinning	10 h 60 °C	Zn(Eu)-MOF@PAN NFM	0–129.3	0.989	2719.6	
20	CA and EDA (CDs); Zn(NO ₃) ₂ ·6H ₂ O, CDs, and 2-methylimidazole (CDs@ZIF-8); Te, NaBH ₄ , CdCl ₂ , MPA (NIR CdTe QDs); CDs@ZIF-8, NIR CdTe QDs, TEOS, NH ₃ ·H ₂ O, APTES (CDs@ZIF-8/CdTe@MIP)	Hydrothermal (CDs);	5 h, 200 °C (CDs); 30 min (CDs@ZIF-8); 1 h, 100 °C (NIR CdTe QDs); 12 h, room temperature (CDs@ZIF-8/CdTe@MIP)	CDs@ZIF-8/CdTe@MIP	1×10^{-7} – 3×10^{-6}	0.995	8×10^{-5}	[73]
		Self-assembly (CDs@ZIF-8); Hydrothermal (NIR CdTe QDs); Mixing (CDs@ZIF-8/CdTe@MIP)			0.05–30			
21	DTPA	Hydrothermal	8 h 200 °C	GQDs	0.5–350	0.962	154	[51]
22	-	-	-	Commercial GQDs	1.44–287.6	0.993	210	[74]

4. Conclusions

4-Nitrophenol (4-NP) is a dangerous pollutant that can harm humans and living organisms owing to its carcinogenicity. This toxic pollutant can be detected using N-

GQDs synthesized using environmentally friendly microplasma technology. Based on the PL intensity decrement with respect to 4-NP concentration, a detection system for 4-NP detection can be established from 0.5 to 150 μM with an LoD of 95.14 nm. The synthesized N-GQDs also demonstrated stable detection of 4-NP over the whole pH range and different temperatures ranging from 10 to 60 $^{\circ}\text{C}$. Our work provides an insight into the sustainable synthesis of N-GQDs in a simple, fast, and environmentally friendly manner using microplasma technology for environmental nanosensors.

Supplementary Materials: The following supporting information can be downloaded at: <https://www.mdpi.com/article/10.3390/chemosensors11070390/s1>. Figure S1. PL spectra of N-GQDs (black), N-GQDs in the presence of 4-NP (red), and 4-NP (blue). Figure S2. Chemical structure of several nitroaromatic compounds. Figure S3. PL quenching ratio of N-GQDs in the presence of 50 μM different nitroaromatic compounds. The excitation used was 330 nm. Figure S4. PL quenching ratio of N-GQDs in the presence of 50 μM 4-NP under different excitation wavelengths.

Author Contributions: M.R.R. and D.K. contributed equally to this work. Conceptualization, D.K.; methodology, D.K.; validation, M.R.R.; formal analysis, M.R.R., D.K. and W.-H.C.; investigation, M.R.R.; resources, W.-H.C.; writing—original draft preparation, M.R.R.; writing—review and editing, D.K. and W.-H.C.; visualization, M.R.R.; supervision, D.K. and W.-H.C.; project administration, W.-H.C.; funding acquisition, W.-H.C. All authors have read and agreed to the published version of the manuscript.

Funding: Financial support is gracefully acknowledged from the National Science and Technology Council (NSTC, grant nos. NSTC 111-2223-E-011-002-MY3, NSTC 111-2628-E-011-002-MY2, NSTC 109-2923-E-011-003-MY3, NSTC 111-2811-E-011-018, NSTC 111-NU-E-011-001-NU).

Institutional Review Board Statement: Not applicable.

Informed Consent Statement: Not applicable.

Data Availability Statement: The experimental data are available upon request from the corresponding author.

Acknowledgments: This work was supported by the National Taiwan University of Science and Technology (NTUST). We also thank Chia-Ying Chien of NSTC (National Taiwan University) for the assistance in the FE-TEM experiment.

Conflicts of Interest: The authors declare no conflict of interest.

References

1. Han, L.; Liu, S.G.; Liang, J.Y.; Ju, Y.J.; Li, N.B.; Luo, H.Q. pH-Mediated Reversible Fluorescence Nanoswitch Based on Inner Filter Effect Induced Fluorescence Quenching for Selective and Visual Detection of 4-Nitrophenol. *J. Hazard. Mater.* **2019**, *362*, 45–52. [[CrossRef](#)] [[PubMed](#)]
2. Bogireddy, N.K.R.; Cruz Silva, R.; Valenzuela, M.A.; Agarwal, V. 4-Nitrophenol Optical Sensing with N Doped Oxidized Carbon Dots. *J. Hazard. Mater.* **2020**, *386*, 121643. [[CrossRef](#)] [[PubMed](#)]
3. Yuan, H.; Yu, J.; Feng, S.; Gong, Y. Highly Photoluminescent pH-Independent Nitrogen-Doped Carbon Dots for Sensitive and Selective Sensing of *p*-Nitrophenol. *RSC Adv.* **2016**, *6*, 15192–15200. [[CrossRef](#)]
4. Bogireddy, N.K.R.; Kiran Kumar, H.A.; Mandal, B.K. Biofabricated Silver Nanoparticles as Green Catalyst in the Degradation of Different Textile Dyes. *J. Environ. Chem. Eng.* **2016**, *4*, 56–64. [[CrossRef](#)]
5. Xiao, N.; Liu, S.G.; Mo, S.; Li, N.; Ju, Y.J.; Ling, Y.; Li, N.B.; Luo, H.Q. Highly Selective Detection of *p*-Nitrophenol Using Fluorescence Assay Based on Boron, Nitrogen Co-Doped Carbon Dots. *Talanta* **2018**, *184*, 184–192. [[CrossRef](#)]
6. Gudipati, N.S.; Vanjari, S.; Korutla, S.; Tammineni, R.R.; Challapalli, S. Electrochemical Detection of 4-Nitrophenol on Nanostructured CuBi₂O₄ with Plausible Mechanism Supported by DFT Calculations. *J. Environ. Chem. Eng.* **2022**, *10*, 108758. [[CrossRef](#)]
7. Mejia, Y.R.; Reddy Bogireddy, N.K. Reduction of 4-Nitrophenol Using Green-Fabricated Metal Nanoparticles. *RSC Adv.* **2022**, *12*, 18661–18675. [[CrossRef](#)]
8. Galeano-Díaz, T.; Guiberteau-Cabanillas, A.; Díez, N.M.; Vázquez, P.P.; López, F.S. Rapid and Sensitive Determination of 4-Nitrophenol Fenitrothion and Parathion-Ethyl by Liquid Chromatography with Electrochemical Detection. *J. Agric. Food Chem.* **2000**, *48*, 4508–4513. [[CrossRef](#)]
9. Herterich, R. Gas Chromatographic Determination of Nitrophenols in Atmospheric Liquid Water and Airborne Particulates. *J. Chromatogr. A* **1991**, *549*, 313–324. [[CrossRef](#)]

10. Kitanovski, Z.; Grgic, I.; Vermeylen, R.; Claeys, M.; Maenhaut, W. Liquid Chromatography Tandem Mass Spectrometry Method for Characterization of Monoaromatic Nitro-Compounds in Atmospheric Particulate Matter. *J. Chromatogr. A* **2012**, *1268*, 35–43. [[CrossRef](#)]
11. Deng, P.; Xu, Z.; Feng, Y.; Li, J. Electrocatalytic Reduction and Determination of *p*-Nitrophenol on Acetylene Black Paste Electrode Coated with Salicylaldehyde-Modified Chitosan. *Sens. Actuators B Chem.* **2012**, *168*, 381–389. [[CrossRef](#)]
12. Li, J.; Kuang, D.; Feng, Y.; Zhang, F.; Xu, Z.; Liu, M. A Graphene Oxide-Based Electrochemical Sensor for Sensitive Determination of 4-Nitrophenol. *J. Hazard. Mater.* **2012**, *201–202*, 250–259. [[CrossRef](#)] [[PubMed](#)]
13. Vilian, A.T.E.; Choe, S.R.; Giribabu, K.; Jang, S.C.; Roh, C.; Huh, Y.S.; Han, Y.K. Pd Nanospheres Decorated Reduced Graphene Oxide with Multi-Functions: Highly Efficient Catalytic Reduction and Ultrasensitive Sensing of Hazardous 4-Nitrophenol Pollutant. *J. Hazard. Mater.* **2017**, *333*, 54–62. [[CrossRef](#)]
14. Ma, X.; Wu, Y.; Devaramani, S.; Zhang, C.; Niu, Q.; Ibrahim Shinger, M.; Li, W.; Shan, D.; Lu, X. Preparation of GO-COOH/AuNPs/ZnAPTPP Nanocomposites Based on the π - π Conjugation: Efficient Interface for Low-Potential Photoelectrochemical Sensing of 4-Nitrophenol. *Talanta* **2018**, *178*, 962–969. [[CrossRef](#)]
15. Mehdiinia, A.; Dadkhah, S.; Baradaran Kayyal, T.; Jabbari, A. Design of a Surface-Immobilized 4-Nitrophenol Molecularly Imprinted Polymer via Pre-Grafting Amino Functional Materials on Magnetic Nanoparticles. *J. Chromatogr. A* **2014**, *1364*, 12–19. [[CrossRef](#)] [[PubMed](#)]
16. Chen, Z.; Niu, Y.; Zhao, S.; Khan, A.; Ling, Z.; Chen, Y.; Liu, P.; Li, X. A Novel Biosensor for *p*-Nitrophenol Based on an Aerobic Anode Microbial Fuel Cell. *Biosens. Bioelectron.* **2016**, *85*, 860–868. [[CrossRef](#)]
17. Yan, K.; Yang, Y.; Zhu, Y.; Zhang, J. Highly Selective Self-Powered Sensing Platform for *p*-Nitrophenol Detection Constructed with a Photocathode-Based Photocatalytic Fuel Cell. *Anal. Chem.* **2017**, *89*, 8599–8603. [[CrossRef](#)]
18. Ponomarenko, L.A.; Schedin, F.; Katsnelson, M.I.; Yang, R.; Hill, E.W.; Novoselov, K.S.; Geim, A.K. Chaotic Dirac Billiard in Graphene Quantum Dots. *Science* **2008**, *320*, 356–358. [[CrossRef](#)]
19. Tshangana, C.S.; Muleja, A.A.; Kuvarega, A.T.; Malefetse, T.J.; Mamba, B.B. The Applications of Graphene Oxide Quantum Dots in the Removal of Emerging Pollutants in Water: An Overview. *J. Water Process. Eng.* **2021**, *43*, 102249. [[CrossRef](#)]
20. Yan, Y.; Gong, J.; Chen, J.; Zeng, Z.; Huang, W.; Pu, K.; Liu, J.; Chen, P. Recent Advances on Graphene Quantum Dots: From Chemistry and Physics to Applications. *Adv. Mater.* **2019**, *31*, e1808283. [[CrossRef](#)]
21. Kurniawan, D.; Weng, R.-J.; Chen, Y.-Y.; Rahardja, M.R.; Nanaricka, Z.C.; Chiang, W.-H. Recent Advances in the Graphene Quantum Dot-Based Biological and Environmental Sensors. *Sens. Actuators Rep.* **2022**, *4*, 100130. [[CrossRef](#)]
22. Bourlinos, A.B.; Trivizas, G.; Karakassides, M.A.; Baikousi, M.; Kouloumpis, A.; Gournis, D.; Bakandritsos, A.; Hola, K.; Kozak, O.; Zboril, R.; et al. Green and Simple Route toward Boron Doped Carbon Dots with Significantly Enhanced Non-Linear Optical Properties. *Carbon* **2015**, *83*, 173–179. [[CrossRef](#)]
23. Li, J.; Jiao, Y.; Feng, L.; Zhong, Y.; Zuo, G.; Xie, A.; Dong, W. Highly N,P-Doped Carbon Dots: Rational Design, Photoluminescence and Cellular Imaging. *Mikrochim. Acta* **2017**, *184*, 2933–2940. [[CrossRef](#)]
24. Li, W.; Zhang, Z.; Kong, B.; Feng, S.; Wang, J.; Wang, L.; Yang, J.; Zhang, F.; Wu, P.; Zhao, D. Simple and Green Synthesis of Nitrogen-Doped Photoluminescent Carbonaceous Nanospheres for Bioimaging. *Angew. Chem. Int. Ed.* **2013**, *52*, 8151–8155. [[CrossRef](#)]
25. Qian, Z.; Shan, X.; Chai, L.; Ma, J.; Chen, J.; Feng, H. Si-Doped Carbon Quantum Dots: A Facile and General Preparation Strategy, Bioimaging Application, and Multifunctional Sensor. *ACS Appl. Mater. Interfaces* **2014**, *6*, 6797–6805. [[CrossRef](#)]
26. Xu, Q.; Pu, P.; Zhao, J.; Dong, C.; Gao, C.; Chen, Y.; Chen, J.; Liu, Y.; Zhou, H. Preparation of Highly Photoluminescent Sulfur-Doped Carbon Dots for Fe(III) Detection. *J. Mater. Chem. A* **2015**, *3*, 542–546. [[CrossRef](#)]
27. Yang, S.; Sun, J.; He, P.; Deng, X.; Wang, Z.; Hu, C.; Ding, G.; Xie, X. Selenium Doped Graphene Quantum Dots as an Ultrasensitive Redox Fluorescent Switch. *Chem. Mater.* **2015**, *27*, 2004–2011. [[CrossRef](#)]
28. Wang, Y.; Hu, A. Carbon Quantum Dots: Synthesis, Properties and Applications. *J. Mater. Chem. C* **2014**, *2*, 6921–6939. [[CrossRef](#)]
29. Atchudan, R.; Edison, T.N.J.I.; Chakradhar, D.; Perumal, S.; Shim, J.-J.; Lee, Y.R. Facile Green Synthesis of Nitrogen-Doped Carbon Dots using Chionanthus Retusus Fruit Extract and Investigation of Their Suitability for Metal Ion Sensing and Biological Applications. *Sens. Actuators B Chem.* **2017**, *246*, 497–509. [[CrossRef](#)]
30. Atchudan, R.; Edison, T.; Lee, Y.R. Nitrogen-Doped Carbon Dots Originating from Unripe Peach for Fluorescent Bioimaging and Electrocatalytic Oxygen Reduction Reaction. *J. Colloid. Interface Sci.* **2016**, *482*, 8–18. [[CrossRef](#)]
31. Edison, T.N.; Atchudan, R.; Sethuraman, M.G.; Shim, J.J.; Lee, Y.R. Microwave Assisted Green Synthesis of Fluorescent N-Doped Carbon Dots: Cytotoxicity and Bio-Imaging Applications. *J. Photochem. Photobiol. B Biol.* **2016**, *161*, 154–161. [[CrossRef](#)] [[PubMed](#)]
32. Edison, T.N.; Atchudan, R.; Shim, J.J.; Kalimuthu, S.; Ahn, B.C.; Lee, Y.R. Turn-Off Fluorescence Sensor for the Detection of Ferric Ion in Water Using Green Synthesized N-Doped Carbon Dots and Its Bio-Imaging. *J. Photochem. Photobiol. B Biol.* **2016**, *158*, 235–242. [[CrossRef](#)] [[PubMed](#)]
33. Atchudan, R.; Edison, T.N.J.I.; Perumal, S.; Vinodh, R.; Lee, Y.R. In-situ Green Synthesis of Nitrogen-Doped Carbon Dots for Bioimaging and TiO₂ Nanoparticles@Nitrogen-doped Carbon Composite for Photocatalytic Degradation of Organic Pollutants. *J. Alloys Compd.* **2018**, *766*, 12–24. [[CrossRef](#)]
34. Du, Y.; Guo, S. Chemically Doped Fluorescent Carbon and Graphene Quantum Dots for Bioimaging, Sensor, Catalytic and Photoelectronic Applications. *Nanoscale* **2016**, *8*, 2532–2543. [[CrossRef](#)]

35. Ghaffarkhah, A.; Hosseini, E.; Kamkar, M.; Sehat, A.A.; Dordanihaghghi, S.; Allahbakhsh, A.; van der Kuur, C.; Arjmand, M. Synthesis, Applications, and Prospects of Graphene Quantum Dots: A Comprehensive Review. *Small* **2022**, *18*, e2102683. [[CrossRef](#)]
36. Bellich, B.; D'Agostino, I.; Semeraro, S.; Gamini, A.; Cesaro, A. "The Good, the Bad and the Ugly" of Chitosans. *Mar. Drugs* **2016**, *14*, 99. [[CrossRef](#)]
37. Nilsen-Nygaard, J.; Strand, S.; Vårum, K.; Draget, K.; Nordgård, C. Chitosan: Gels and Interfacial Properties. *Polymers* **2015**, *7*, 552–579. [[CrossRef](#)]
38. Bruggeman, P.J.; Kushner, M.J.; Locke, B.R.; Gardeniers, J.G.E.; Graham, W.G.; Graves, D.B.; Hofman-Caris, R.C.H.M.; Maric, D.; Reid, J.P.; Ceriani, E.; et al. Plasma–Liquid Interactions: A Review and Roadmap. *Plasma Sources Sci. Technol.* **2016**, *25*, 053002. [[CrossRef](#)]
39. Chiang, W.-H.; Richmonds, C.; Sankaran, R.M. Continuous-Flow, Atmospheric-Pressure Microplasmas: A Versatile Source for Metal Nanoparticle Synthesis in the Gas or Liquid Phase. *Plasma Sources Sci. Technol.* **2010**, *19*, 034011. [[CrossRef](#)]
40. Mariotti, D.; Patel, J.; Švrček, V.; Maguire, P. Plasma-Liquid Interactions at Atmospheric Pressure for Nanomaterials Synthesis and Surface Engineering. *Plasma Process Polym.* **2012**, *9*, 1074–1085. [[CrossRef](#)]
41. Mariotti, D.a.R.M.S. Microplasmas for Nanomaterials Synthesis. *J. Phys. D* **2010**, *43*, 323001. [[CrossRef](#)]
42. Yang, J.-S.; Pai, D.Z.; Chiang, W.-H. Microplasma-Enhanced Synthesis of Colloidal Graphene Quantum Dots at Ambient Conditions. *Carbon* **2019**, *153*, 315–319. [[CrossRef](#)]
43. Chiang, W.-H.; Mariotti, D.; Sankaran, R.M.; Eden, J.G.; Ostrikov, K.K. Microplasmas for Advanced Materials and Devices. *Adv. Mater.* **2020**, *32*, e1905508. [[CrossRef](#)] [[PubMed](#)]
44. Kurniawan, D.; Rahardja, M.R.; Fedotov, P.V.; Obratsova, E.D.; Ostrikov, K.K.; Chiang, W.-H. Plasma-Bioresource-Derived Multifunctional Porous NGQD/AuNP Nanocomposites for Water Monitoring and Purification. *Chem. Eng. J.* **2023**, *451*, 139083. [[CrossRef](#)]
45. Yeh, T.F.; Huang, W.L.; Chung, C.J.; Chiang, I.T.; Chen, L.C.; Chang, H.Y.; Su, W.C.; Cheng, C.; Chen, S.J.; Teng, H. Elucidating Quantum Confinement in Graphene Oxide Dots Based on Excitation-Wavelength-Independent Photoluminescence. *J. Phys. Chem. Lett.* **2016**, *7*, 2087–2092. [[CrossRef](#)]
46. Jiao, Y.; Gong, X.; Han, H.; Gao, Y.; Lu, W.; Liu, Y.; Xian, M.; Shuang, S.; Dong, C. Facile Synthesis of Orange Fluorescence Carbon Dots with Excitation Independent Emission for pH Sensing and Cellular Imaging. *Anal. Chim. Acta* **2018**, *1042*, 125–132. [[CrossRef](#)]
47. Kurniawan, D.; Sharma, N.; Rahardja, M.R.; Cheng, Y.Y.; Chen, Y.T.; Wu, G.X.; Yeh, Y.Y.; Yeh, P.C.; Ostrikov, K.K.; Chiang, W.H. Plasma Nanoengineering of Bioresource-Derived Graphene Quantum Dots as Ultrasensitive Environmental Nanoprobes. *ACS Appl. Mater. Interfaces* **2022**, *14*, 52289–52300. [[CrossRef](#)]
48. Kurniawan, D.; Chiang, W.-H. Microplasma-Enabled Colloidal Nitrogen-Doped Graphene Quantum Dots for Broad-Range Fluorescent pH Sensors. *Carbon* **2020**, *167*, 675–684. [[CrossRef](#)]
49. Das, R.; Parveen, S.; Bora, A.; Giri, P.K. Origin of High Photoluminescence Yield and High SERS Sensitivity of Nitrogen-Doped Graphene Quantum Dots. *Carbon* **2020**, *160*, 273–286. [[CrossRef](#)]
50. Zhang, H.; Yuan, Z.; Wang, M.; Zhu, L.; Cheng, X.; Cao, D.; Guan, R.; Zhou, C. Application of Graphene Quantum Dots in the Detection of Hg^{2+} and ClO^- and Analysis of Detection Mechanism. *Diam. Relat. Mater.* **2021**, *117*, 108454. [[CrossRef](#)]
51. Soni, H.; Pamidimukkala, P. Liquid Crystalline Multilayer Graphene Quantum Dots with Hackelite Structures: Characterisation and Application for Sensing Nitrophenols. *Sens. Actuators B Chem.* **2018**, *268*, 100–107. [[CrossRef](#)]
52. Chen, C.; Hildebrandt, N. Resonance Energy Transfer to Gold Nanoparticles: NSET Defeats FRET. *Trends Anal. Chem.* **2020**, *123*, 115748. [[CrossRef](#)]
53. Zu, F.; Yan, F.; Bai, Z.; Xu, J.; Wang, Y.; Huang, Y.; Zhou, X. The Quenching of the Fluorescence of Carbon Dots: A Review on Mechanisms and Applications. *Microchim. Acta* **2017**, *184*, 1899–1914. [[CrossRef](#)]
54. Anh, N.T.N.; Chang, P.-Y.; Doong, R.-A. Sulfur-Doped Graphene Quantum Dot-Based Paper Sensor for Highly Sensitive and Selective Detection of 4-Nitrophenol in Contaminated Water and Wastewater. *RSC Adv.* **2019**, *9*, 26588–26597.
55. Sun, P.P.; Araud, E.M.; Huang, C.; Shen, Y.; Monroy, G.L.; Zhong, S.; Tong, Z.; Boppart, S.A.; Eden, J.G.; Nguyen, T.H. Disintegration of Simulated Drinking Water Biofilms with Arrays of Microchannel Plasma Jets. *NPJ Biofilms Microbiomes* **2018**, *4*, 24. [[CrossRef](#)]
56. Lin, L.; Pho, H.Q.; Zong, L.; Li, S.; Pourali, N.; Rebrov, E.; Tran, N.N.; Ostrikov, K.K.; Hessel, V. Microfluidic Plasmas: Novel Technique for Chemistry and Chemical Engineering. *Chem. Eng. J.* **2021**, *417*, 129355. [[CrossRef](#)]
57. Chatzimarkou, A.; Chatzimitakos, T.G.; Kasouni, A.; Sygellou, L.; Avgeropoulos, A.; Stalikas, C.D. Selective FRET-Based Sensing of 4-Nitrophenol and Cell Imaging Capitalizing on the Fluorescent Properties of Carbon Nanodots from Apple Seeds. *Sens. Actuators B Chem.* **2018**, *258*, 1152–1160. [[CrossRef](#)]
58. Dai, H.; Deng, Z.; Zeng, Y.; Zhang, J.; Yang, Y.; Ma, Q.; Hu, W.; Guo, L.; Li, L.; Wan, S.; et al. Highly Sensitive Determination of 4-Nitrophenol with Coumarin-Based Fluorescent Molecularly Imprinted Poly (Ionic Liquid). *J. Hazard. Mater.* **2020**, *398*, 122854. [[CrossRef](#)]
59. Dang, D.K.; Sundaram, C.; Ngo, Y.-L.T.; Choi, W.M.; Chung, J.S.; Kim, E.J.; Hur, S.H. Pyromellitic Acid-Derived Highly Fluorescent N-Doped Carbon Dots for the Sensitive and Selective Determination of 4-Nitrophenol. *Dye. Pigm.* **2019**, *165*, 327–334. [[CrossRef](#)]

60. Shu, T.; Wang, J.; Lin, X.; Zhou, Z.; Liang, F.; Su, L.; Zhang, X. Dual-Emissive Gold Nanoclusters for Label-Free and Separation-Free Ratiometric Fluorescence Sensing of 4-Nitrophenol Based on the Inner Filter Effect. *J. Mater. Chem. C* **2018**, *6*, 5033–5038. [[CrossRef](#)]
61. Wang, F.; Fu, X.; Chai, X.; Han, Q.; Wang, H.; Hao, Q. Highly Selective Fluorometric Detection of para-Nitrophenol from Its Isomers by Nitrogen-Doped Graphene Quantum Dots. *Microchem. J.* **2021**, *168*, 106389. [[CrossRef](#)]
62. Wang, X.; Zuo, Y.; Feng, S. Ultrasensitive Polysiloxane-Based Fluorescent Probes for Selectively Detecting of 4-Nitrophenol and Their Application in Paper Sensors. *Mater. Today Commun.* **2020**, *25*, 101570. [[CrossRef](#)]
63. Yang, J.-M.; Hu, X.-W.; Liu, Y.-X.; Zhang, W. Fabrication of a Carbon Quantum Dots-Immobilized Zirconium-Based Metal-Organic Framework Composite Fluorescence Sensor for Highly Sensitive Detection of 4-Nitrophenol. *Microporous Mesoporous Mater.* **2019**, *274*, 149–154. [[CrossRef](#)]
64. Zhang, S.; Zhang, D.; Ding, Y.; Hua, J.; Tang, B.; Ji, X.; Zhang, Q.; Wei, Y.; Qin, K.; Li, B. Bacteria-Derived Fluorescent Carbon Dots for Highly Selective Detection of *p*-Nitrophenol and Bioimaging. *Analyst* **2019**, *144*, 5497–5503. [[CrossRef](#)] [[PubMed](#)]
65. Venugopalan, P.; Vidya, N. Microwave Assisted Green Synthesis of Carbon Dots from Sweet Flag (*Acorus calamus*) for Fluorescent Sensing of 4-Nitrophenol. *J. Photochem. Photobiol. A* **2023**, *439*, 114625. [[CrossRef](#)]
66. Chen, J.; Xia, X.; Li, P.; Yu, H.; Xie, Y.; Guo, Y.; Yao, W.; Qian, H.; Cheng, Y. Crayfish Shells-Derived Carbon Dots as a Fluorescence Sensor for the Selective Detection of 4-Nitrophenol. *Food Agric. Immunol.* **2023**, *34*, 36–47. [[CrossRef](#)]
67. Wang, K.; Tan, L.; Zhang, Y.; Zhang, D.; Wang, N.; Wang, J. A Molecular Imprinted Fluorescence Sensor Based on Carbon Quantum Dots for Selective Detection of 4-Nitrophenol in Aqueous Environments. *Mar. Pollut. Bull.* **2023**, *187*, 114587. [[CrossRef](#)]
68. Wang, H.; Ma, S.; Sun, Y.; Gao, M.; Wang, X. Detection of 4-Nitrophenol by a Naphthene Carboxylic Acid-Based Fluorescent Dicationic Ionic Liquid in Environmental Waters and Soils. *Microchem. J.* **2023**, *190*, 108720. [[CrossRef](#)]
69. Luo, K.; Luo, X.; Wu, Y.; Liang, Z.; Kang, X.; Wen, Y. Synthesis of Graphene Quantum Dots with Temperature-Sensitive Properties from Sea Rice for Rapid and Highly Selective Detection of 4-Nitrophenol. *Diam. Relat. Mater.* **2023**, *135*, 109849. [[CrossRef](#)]
70. Wang, X.; Zhu, R.; Wang, X.; Liu, F.; Gao, Y.; Guan, R.; Chen, Y. Flexible and Washable CDs@Eu-MOFs/PVDF Multifunctional Thin Films as Highly Selective Sensing for Nitrobenzene and 4-Nitrophenol. *Inorg. Chem. Commun.* **2023**, *149*, 110423. [[CrossRef](#)]
71. Han, Y.; Wang, Y.; Zhang, H.; Zhao, L.; Qiu, H. Facile Synthesis of Yellow-Green Fluorescent Silicon Nanoparticles and Their Application in Detection of Nitrophenol Isomers. *Talanta* **2023**, *257*, 124347. [[CrossRef](#)] [[PubMed](#)]
72. Chen, M.; Shao, R.; Wang, Q.; Gao, Y.; Ma, Y.; Guan, R.; Yang, T. Eu Doped Zn-MOF Nanofiber Fluorescent Membrane and Its Multifunctional Detection of Nitroaromatic Compounds and Fe³⁺. *Polyhedron* **2023**, *235*, 116363. [[CrossRef](#)]
73. Fu, J.; Zhou, S.; Zhao, P.; Wu, X.; Tang, S.; Chen, S.; Yang, Z.; Zhang, Z. A Dual-Response Ratiometric Fluorescence Imprinted Sensor Based on Metal-Organic Frameworks for Ultrasensitive Visual Detection of 4-Nitrophenol in Environments. *Biosens. Bioelectron.* **2022**, *198*, 113848. [[CrossRef](#)] [[PubMed](#)]
74. El-Shaheny, R.; Yoshida, S.; Fuchigami, T. Graphene Quantum Dots as a Nanoprobe for Analysis of *o*- and *p*-Nitrophenols in Environmental Water Adopting Conventional Fluorometry and Smartphone Image Processing-Assisted Paper-Based Analytical Device. In-Depth Study of Sensing Mechanisms. *Microchem. J.* **2020**, *158*, 105241. [[CrossRef](#)]

Disclaimer/Publisher's Note: The statements, opinions and data contained in all publications are solely those of the individual author(s) and contributor(s) and not of MDPI and/or the editor(s). MDPI and/or the editor(s) disclaim responsibility for any injury to people or property resulting from any ideas, methods, instructions or products referred to in the content.